

Dupleich, Diego; Müller, Robert; Landmann, Markus; Shinwasusin, Ek-Amorn; Saito, Kentaro; Takada, Jun-ichi; Luo, Jian; Thomä, Reiner; Del Galdo, Giovanni:

Multi-band propagation and radio channel characterization in street canyon scenarios for 5G and beyond

Original published in: IEEE access / Institute of Electrical and Electronics Engineers New York, NY : IEEE. - 7 (2019), p. 160385-160396.
Original published: 2019-10-22
ISSN: 2169-3536
DOI: [10.1109/ACCESS.2019.2948869](https://doi.org/10.1109/ACCESS.2019.2948869)
[Visited: 2019-12-03]



This work is licensed under a [Creative Commons Attribution 4.0 International license](https://creativecommons.org/licenses/by/4.0/). To view a copy of this license, visit <http://creativecommons.org/licenses/by/4.0/>

Received August 9, 2019, accepted September 20, 2019, date of publication October 22, 2019, date of current version November 14, 2019.

Digital Object Identifier 10.1109/ACCESS.2019.2948869

Multi-Band Propagation and Radio Channel Characterization in Street Canyon Scenarios for 5G and Beyond

DIEGO DUPELEICH¹, ROBERT MÜLLER¹, MARKUS LANDMANN², EK-AMORN SHINWASUSIN³,
KENTARO SAITO³, JUN-ICHI TAKADA³, JIAN LUO⁴, REINER THOMÄ¹,
AND GIOVANNI DEL GALDO¹

¹Elektronische Messtechnik und Signalverarbeitung, Technische Universität Ilmenau, 98693 Ilmenau, Germany

²Elektronische Messtechnik und Signalverarbeitung, Fraunhofer Institute for Integrated Circuits, 98693 Ilmenau, Germany

³Tokyo Institute of Technology, Tokyo 152-8550, Japan

⁴Huawei German Research Center, Munich, Germany.

Corresponding author: Diego Dupleich (diego.dupleich@tu-ilmenau.de)

This work was supported in part by the German Academic Exchange Service (DAAD, Projektbezogener Personenaustausch mit Japan 2017), in part by the Article Processing Charge by the German Research Foundation (DFG), and in part by the Open Access Publication Fund of the Technische Universität Ilmenau.

ABSTRACT Radio access at mm-waves has been subject of intensive research in the latest years. However, within the initial deployment of 5G, mm-waves are still relegated and there is a generalized idea that the mm-wave channel for radio access, in comparison to the sub-6 GHz channel, is not only sparse but also troublesome for outdoor applications. In the present paper we introduce simultaneous multi-band measurements comparing the sub-6 GHz with the mm-waves channel at 30 GHz and 60 GHz in street canyon scenarios using the same measurement equipment in Germany and Japan. An analysis on the propagation and radio channel characteristics shows that the mm-waves channel offers similar opportunities as the sub-6 GHz. Consequently, the challenge relies on the design of an adequate radio interface matching the channel characteristics. In that regard, aspects as the location of clusters and spatial consistency gain importance within geometry-based stochastic channel models (GBSCMs). The analysis of the large-scale parameters (LSPs) has shown a large influence of the geometry of the scenario on the channel, encouraging the introduction of deterministic modelling components within GBSCMs targeting these scenarios.

INDEX TERMS Multi-band measurements, mm-waves, quasi-deterministic channel modelling, street canyon, sub-6 GHz, 5G.

I. INTRODUCTION

The large blocks of free spectrum available at mm-waves make these frequency bands very suitable to provide the necessary bandwidths to meet the requirements of future wireless technologies [1]. Therefore, there have been efforts on an accurate characterization of the channel at mm-waves, as shown in standardization bodies as the 3GPP [2], scientific communities [3], and consortia as MiWEBA [4], the mmMAGIC project [5], and METIS [6].

However, the increased isotropic free-space path-loss and penetration loss limits the access range of mm-waves in

The associate editor coordinating the review of this manuscript and approving it for publication was Ke Guan¹.

outdoor scenarios. Consequently, high directive antennas have to be deployed at the base station (BS) and user equipment (UE) to compensate path-loss. As the antenna element size is inversely proportional to the carrier frequency, multiple antennas can be packed in small volumes and electrically large arrays with the aforementioned needed gains can be achieved. While fully digital beam-forming is usually employed at sub-6 GHz due to its high flexibility and capacity gains [7], the large number of antennas and system bandwidth in mm-wave systems makes it expensive in terms of cost and energy consumption [8]. Therefore, the current trend is towards hybrid analog/digital implementations, in which the signal of multiple antennas are previously combined in the analog domain to compensate path-loss, and then derived

to the digital interface [9]. This results in high directive radio channels with the need of adaptive beam-forming and tracking in mobile environments.

Therefore, compared to sub-6 GHz systems, the radio channel at mm-waves differs substantially to the propagation channel. At sub-6 GHz, the digital interfaces are usually connected directly to low gain antennas, sampling a radio channel that approximates the isotropic propagation channel. Because of the low directivity, multi-path propagation produces large spreads of signals in the delay domain, visible in figures as delay spread (DS) and Doppler Spread. Moreover, narrow application bandwidths reduce the capability of resolving these multi-path components (MPCs) in the delay domain, which results in deep small scale fading. Therefore, stochastic models are very suitable to describe the sub-6 GHz propagation and radio channel due to the low resolution of the systems in delay and angular domain.

On the other hand, digital interfaces sample a directive radio channel at mm-wave systems, which is only a portion of the isotropic propagation channel. Several clusters of MPCs are filtered out and signals are less spread in the delay and Doppler domain. In addition, the extended application bandwidth enables the resolution of MPCs in the delay domain, reducing fading as shown by measurements in [10]. The increased resolution of the system allows determining intra-cluster propagation parameters as polarization [11], [12], DS, and angular spreads (ASs) [13]. Therefore, channel models at mm-waves need to be updated considering those aspects.

While pure deterministic propagation models as ray-tracing are more suitable to address features as spatial consistency and provide a rigorous location of scatterers and intra-cluster properties, the results are very site specific, which limits the flexibility of the model to test different situations. Therefore, geometry-based stochastic channel models (GBSCMs) offer a good compromise between accuracy and ease of generate multiple channels. GBSCMs can be divided into system-level and cluster-level [14]. Within the first ones we can find the WINNER II [15] and spatial channel model (SCM) family in 3GPP models (and the ones based on the 3GPP recommendations as the mmMagic [5] and stochastic models within METIS [6]). In those models, the generation of the MPCs is governed by the large-scale parameters (LSPs), guaranteeing their statistics in every instance. However, the MPCs are not related to particular scatterers. Therefore, there is not a genuine consistency between time of arrival (TOA) and direction of departure (DOD)/direction of arrival (DOA). This burdens the implementation of spatial consistency and continuous displacements over intervals larger than the auto-correlation distance. Thus, testing of beam-forming and tracking is not realistic.

On the other hand, cluster-level models as COST-2100 [14], place scattering objects in the environment on a particular geometry (circle, ellipsoid, or 2D/3D coordinates) and the randomization of the model relies on the application of visibility regions. Consequently, in these models, the statistics of LSPs are not guaranteed, since they depend on the location

of the scatterers and their scattering characteristics (ASs, reflected power, polarization, etc.). A similar methodology is followed in the quasi-deterministic approach introduced in [16], in which the channel is composed by stochastic and deterministic clusters. Moreover, map-based hybrid ray-tracing models in METIS [6] also base the deterministic clusters on pre-loaded or randomly generated maps.

Besides, multiple radio interfaces at different frequencies will co-exist in the same BS and UE, e.g. current sub-6 GHz long-term evolution (LTE) and future mm-wave radio access. Hence, cooperative inter-band algorithms can be developed to ease channel estimation. A coarse DOA can be done at sub-6 GHz and used as starting point for the fine beam-tracking/steering at mm-waves [17]. Therefore, channel models need to be extended to cover multi-band simulations with inter-band correlations to test such algorithms. In that regard, standardization groups and consortia have been working on multi-band channel models based on measurements, as the ones presented in [5], [6], and [18].

Valuable multi-band measurements in different environments and scenarios can be found in the literature. Path-loss, DS, and azimuth spread of arrival (ASA) at 28 GHz and 140 GHz are compared in a shopping mall scenario in [19]. Path-loss and DS in outdoor measurements covering the spectrum from 0.8 GHz to 73 GHz in a residential area in England can be found in [20]. While path-loss in macro-cell environments in different cities in Japan is analysed in [21], [22] presents a similar work at 38 GHz in Austin, USA. Street canyon measurements at mm-waves in New York can be found in [23] and [24], and a comparison with measurements in Korea is presented in [25]. Similarly, multi-band measurements at 10 GHz and 60 GHz in street canyon scenario in Germany can be found in [26]. However, many of these multi-band measurements have been conducted using channel sounders having different bandwidths and antenna set-ups with different characteristics in each measured band, making a fair comparison of pure propagation aspects not possible. In that regard, we have introduced a simultaneous multi-band channel sounding architecture covering the sub-6 GHz and mm-waves in [27]. Measurements in a large indoor hall under different visibility conditions have shown high similarities in the different bands and a large inter-band correlation on the LSPs in [28]. Related measurements in V2V scenarios have shown also similar results in [29].

In this paper we present simultaneous double-directional ultra-wideband multi-band measurements at 6.75 GHz (from 3.375 GHz to 10.125 GHz), 30 GHz (from 30.375 GHz to 37.125 GHz), and 60 GHz (from 57.375 GHz to 64.125 GHz) in a line-of-sight (LOS) street canyon scenario in two different locations with differences in the architecture. Firstly, we compare propagation aspects as scattering in the different bands and scenarios, in order to identify the opportunities that the mm-waves channel offers, using the sub-6 GHz as a reference. Secondly, we analyse the influence of the architecture on the LSPs. The objective is to identify the presence and relevance of deterministic scatterers, showing



FIGURE 1. View from the TX into the street canyon in the Ilmenau scenario.

their influence in the propagation channel and the limitations of the current system-level based GBSCMs to test tracking and beam-forming applications. Finally, we analyse the radio-channel at mm-waves assuming systems aspects as directivity in aligned-LOS (ALOS) and non-aligned-LOS (NALOS).

II. SIMULTANEOUS MULTI-BAND MEASUREMENTS

A. MULTI-BAND CHANNEL SOUNDING

Simultaneous multi-band measurements allow the comparison of propagation and radio channel in different bands. The same absolute bandwidth is utilized in the different bands to have the same delay (spatial) resolution, even if this is not the final application bandwidth.

The multi-band dual-polarized ultra-wideband channel sounder (CS) consists of three 12-bit M-sequence units operating at a clock frequency of 6.75 GHz, which also defines the absolute measurement bandwidth to $B = 6.75$ GHz, [30]. The M-sequence units are connected independently to in-house developed up- and down-converters to the carrier frequencies f_c of 6.75 GHz, 33.75 GHz, and 60.75 GHz. For sake of simplicity, we name the bands along this paper as 6.75 GHz, 30 GHz, and 60 GHz, respectively. For comparison, we also refer to the 6.75 GHz measurements as sub-6 GHz, since due to the large bandwidth, we are also covering down to the 4 GHz bands (3.375 GHz).

The antennas for the different bands are mounted on the same CS but in different directions. Since the CS is mounted over a controllable positioner that can rotate in azimuth and elevation, the measurements are taken synchronously per-band. After a complete rotation in azimuth, the measurements can be re-organized with the same angular reference system.

A camera with a view angle of $\approx 60^\circ$ is installed in one of the sides of the CS, taking a picture at every measurement point. These pictures are used later to identify scatterers. More details on the multi-band CS and applications can be found in [27].

The output of the CS is a multi-dimensional array containing the time domain channel impulse response (CIR) with respect to the vertical and horizontal polarizations, azimuth and elevation scans at TX and RX,

$$h_{f_c}^p(l\Delta\tau, i\Delta\phi_{RX}, j\Delta\theta_{RX}, m\Delta\phi_{TX}, n\Delta\theta_{TX}) \in \mathbb{C}, \quad (1)$$

where $p = \{\varphi\phi, \varphi\theta, \vartheta\phi, \vartheta\theta\}$ is the TX-RX polarization, $\Delta\tau = \frac{1}{B}$ is the delay domain resolution, $\Delta\phi_{RX, TX}$ is the

scanning step in the azimuth domain, and $\Delta\theta_{TX, RX}$ is the scanning step in the elevation domain. For sake of simplicity, (1) is rewritten as

$$h_{f_c}^p(\tau, \phi, \theta, \varphi, \vartheta), \quad (2)$$

where $\tau = l\Delta\tau$, $\phi = i\Delta\phi_{RX}$, $\theta = j\Delta\theta_{RX}$, $\varphi = m\Delta\phi_{TX}$, and $\vartheta = n\Delta\theta_{TX}$.

The noise floor is estimated on every CIR and all the samples lower than the noise floor plus a margin of 10 dB are set to zero. Since polarization is not addressed in this work, unless otherwise is indicated, the absolute squared values of the samples are summed over all the polarizations.

B. SCENARIOS AND MEASUREMENT SET-UP

We have performed measurements using the same channel sounder in two different street canyon scenarios in Ilmenau and Tokyo. While the Ilmenau scenario consists of a wide street with multiple buildings with irregular shapes (also quite typical in big cities in Germany) and more vegetation, the Tokyo scenario is characterized by a narrower street with higher buildings presenting a more regular shape and no vegetation. In both cases, there was a building at the end of the street (Building B in Ilmenau and Building D in Tokyo, see Fig. 1). The results of the measurements can be directly compared since exactly the same equipment was used in both locations. In this way, it is possible to isolate and analyse the influence of the environment on the propagation channel. The scenario was closed to keep the environment unchanged and the stationary of the channel.

In this set of measurements, we have used at the TX and RX sides three different dual-polarized horn antennas with 30° half-power beamwidth (HPBW). Therefore, the scanning steps was set to $\Delta\theta_{TX, RX} = \Delta\phi_{TX, RX} = 30^\circ$. The antennas have been selected to have a radiation pattern as similar as possible in the different bands. However, the patterns are not constant over frequency, and some differences can be found due to the large measurement bandwidth. Since the antennas are not de-embedded from the measurements, the results are antenna dependent.

1) ILMENAU, GERMANY

The measurements were conducted in the campus of the Technische Universität Ilmenau (TUIL). The TX was located

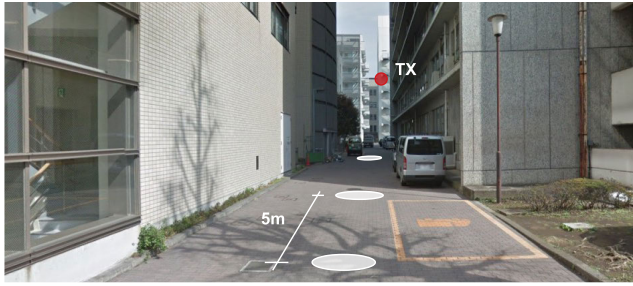


FIGURE 2. View from position RX13 towards the TX in the street canyon in the Tokyo scenario.

in the fire scape staircase of the tallest building emulating a base station at approximately 17 m height, as shown in Fig. 1. On the other side, the RX was located in LOS at 1.6 m height over the street in 13 different positions separated 10 m away from each other, as shown in Fig. 3a. Unfortunately, the position RX4 was corrupted and is not considered in the analysis. At the TX, the azimuth was scanned from -90° to 90° , and the elevation from from -45° to -15° . On the other side, at the RX, the azimuth was scanned from -180° to 150° , and the elevation from from -30° to 30° .

2) TOKYO, JAPAN

The measurements were performed at the campus of the Tokyo University of Technology. The two mm-waves bands were measured simultaneously at 30 GHz and 60 GHz with the same set-up used in Ilmenau. The TX was located at approximately 17.5 m height in the staircase pointing in the direction of the street canyon, as shown in Fig. 2. The RX was placed in 14 different positions separated 5 m away at a height of 1.6 m (see Fig. 3b). At the TX, the azimuth was scanned from -90° to 90° , and the elevation from from -60° to 0° . On the other side, the azimuth was scanned at the RX from -150° to 180° , and the elevation from -30° to 30° .

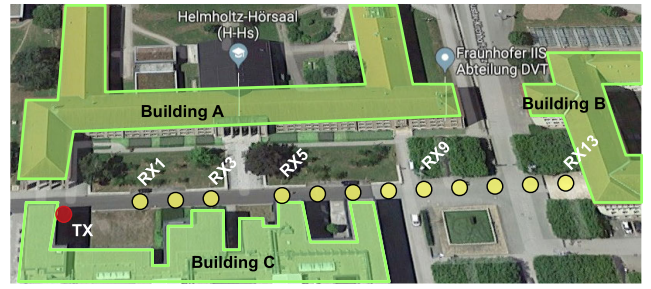
III. ESTIMATION OF SPREAD FUNCTIONS AND LARGE SCALE PARAMETERS FROM DIRECTIVE SCANS

A. TIME-DELAY DOMAIN ANALYSIS

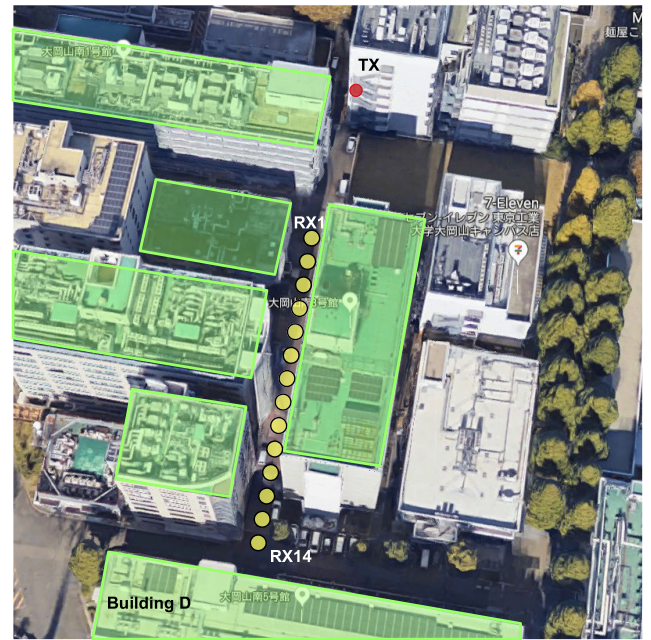
The propagation characteristics in the time-delay domain are represented by the time-delay spread function and RMS DS considering isotropic radiators. Since measurements with directive antennas are mandatory to compensate path-loss, isotropic characteristics with this set-up can only be studied by synthesizing an omni-directional pattern from these directive scans. Hence, the synthetic omni-directional power delay profile (PDP) is calculated as

$$PDP_{SO}(\tau) = \sum_{\forall \phi, \forall \theta, \forall \varphi, \forall \vartheta, \forall \varrho} |h_{fc}^p(\tau, \phi, \theta, \varphi, \vartheta)|^2. \quad (3)$$

On the other hand, the time-delay spread function of the antenna dependent radio channel (similar to beam-forming)



(a)



(b)

FIGURE 3. TX and RX positions in (a) Ilmenau, and (b) Tokyo.

is calculated as

$$PDP_{RC}(\tau) = \sum_{\forall p} |h_{fc}^p(\tau, \phi_i, \theta_j, \varphi_m, \vartheta_n)|^2, \quad (4)$$

where i, j, m , and n are a single TX-RX directional measurement point. The PDP_{SO} intends to characterize the dispersion of the propagation channel in the time domain, independent from the antennas. On the other hand, the PDP_{RC} characterizes the time dispersion considering a beam-former with the capability of steering a beam with 30° HPBW.

The DS is calculated applying a dynamic range (DR) of 20 dB in the $PDP_{SO/RC}$ from (3) or (4):

$$DS_{SO/RC} = \sqrt{\frac{\sum_{\forall \tau} \tau^2 PDP_{SO/RC}(\tau)}{\sum_{\forall \tau} PDP_{SO/RC}(\tau)} - \left(\frac{\sum_{\forall \tau} \tau PDP_{SO/RC}(\tau)}{\sum_{\forall \tau} PDP_{SO/RC}(\tau)} \right)^2}. \quad (5)$$

The DS depends on the DR, bandwidth, and directivity. One of the advantages of this set-up is that the measurements are carried out with the same absolute bandwidth, allowing a fair comparison between the different bands. However, it worth to notice that small differences on the power of MPCs

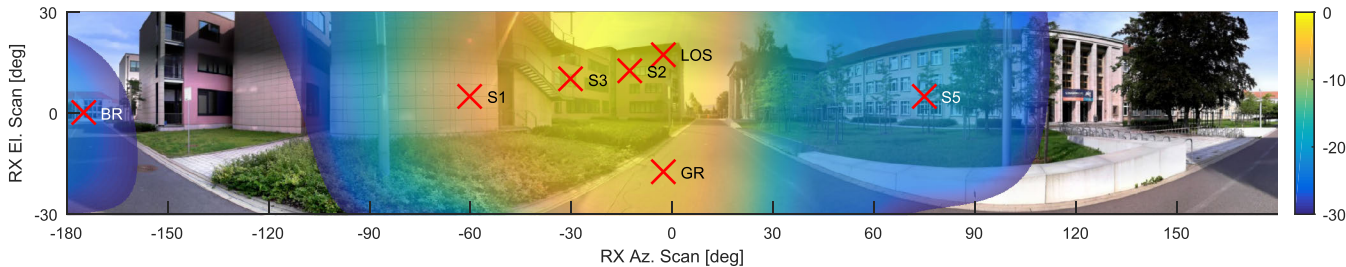


FIGURE 4. PAEP at 60 GHz in RX3 in Ilmenau over the panorama taken by the channel sounder.

in the different measured bands originate large fluctuations on the DSs values. Especially, in those reflections arriving the latest, which can be distinctly present or filtered out in the different bands by the considered DR. Therefore, the calculated absolute value of the per-position and per-band DS is not so relevant as the inter-band trend they follow in the different positions.

B. ANGULAR DOMAIN ANALYSIS

The analysis in the angular domain is performed by condensing the time-delay domain contributions in each directive scan. The marginal power azimuth/elevation profile (PAEP) is calculated by summing up the power in the different directive scans on the other side of the link. Example, the PAEP at RX is calculated as

$$PAEP_{RX}(\phi, \theta) = \sum_{\forall \rho, \forall \tau, \forall \varphi, \forall \vartheta} |h_{fc}^{\rho}(\tau, \phi, \theta, \varphi, \vartheta)|^2. \quad (6)$$

The marginal power azimuth profile (PAP) characterizes the channel in the azimuth domain at TX or RX,

$$PAP_{RX}(\phi) = \sum_{\forall \rho, \forall \tau, \forall \theta, \forall \varphi, \forall \vartheta} |h_{fc}^{\rho}(\tau, \phi, \theta, \varphi, \vartheta)|^2. \quad (7)$$

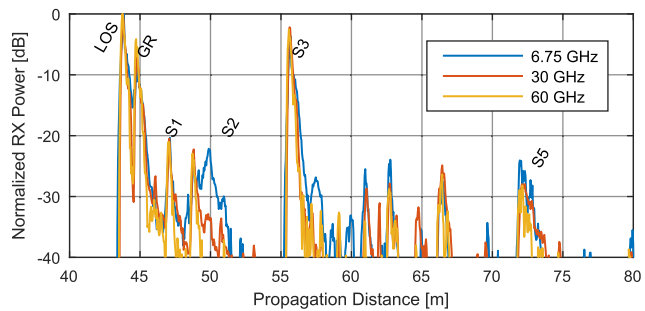
The ASs are estimated similarly as DS, but replacing PDP(τ) by PAP_{TX/RX}(ϕ/φ) in (5).

IV. MULTI-BAND PROPAGATION ANALYSIS

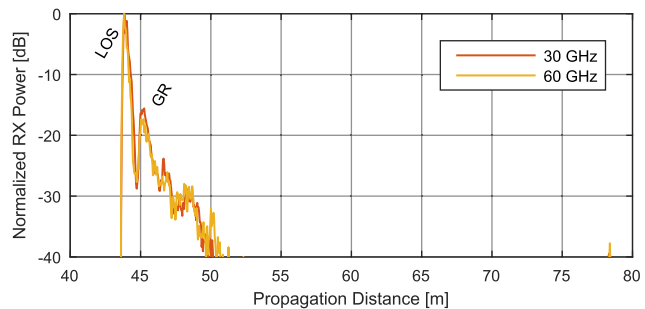
A. ENVIRONMENT CHARACTERIZATION FROM MEASUREMENTS

Different scatterers were identified using the scanning direction, time-delay of the observed peaks in the PDP, and pictures taken by the channel sounder. As an example, the PAEP at 60 GHz in the position RX3 in Ilmenau is overlaid in the panorama picture in Fig. 4. The main scatterers are indicated in the angular domain and later labelled in the multi-band synthetic omni-directional PDP in Fig. 5a.

Apart from scatterers as S2, we can observe that the majority and most relevant components are present with similar power at sub-6 GHz and in the mm-wave bands. Remarkable is scatterer S3, which is a reflection on the Building C in Fig. 1, appears approx. 3 dB lower than the LOS. Similarly, Fig. 5b shows the multi-band synthetic omni-directional PDP in the position RX3 in Tokyo. The ground reflection (GR) is also resolved in the time-delay domain, but compared to



(a)



(b)

FIGURE 5. Detail of the multi-band synthetic omni-directional PDP in the position RX3 in (a) Ilmenau, and (b) Tokyo.

the Ilmenau scenario, the relative power of GR to the LOS component is lower. Further discussions on GR follow in Section V-A.

In addition, the influence of the street width is noticeable in the spread of the signal in delay in Fig. 5: within a narrow street, side reflections arrive closer to the LOS component (Tokyo), and with a wider street, the side reflections arrive later in the PDP (Ilmenau).

B. TIME-DELAY DOMAIN CHARACTERIZATION

The normalized synthetic omni-directional PDP and normalized per-position total RX power in the different scenarios at 30 GHz can be observed in Fig. 6. The evolution of the channel shows the increase of power (relative to the LOS component) of the reflection from the building at the end of the street: Building B and D in Ilmenau and Tokyo, respectively (see Fig. 3), and from multiple scatterers located also behind the RX.

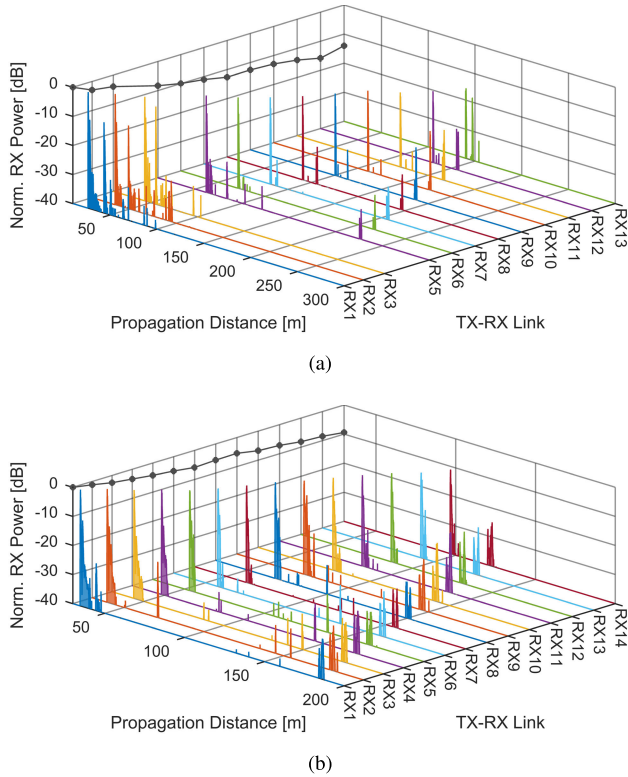


FIGURE 6. Per-position synthetic omni-directional PDP at 30 GHz in (a) Ilmenau (wide canyon), and (b) Tokyo (narrow canyon).

The multi-band per position DS in the Ilmenau and Tokyo scenarios are shown in Fig. 7a and 7b, respectively, and the mean and standard deviation summarized in Table 2. In average, the DS is shorter in Tokyo than in Ilmenau. We can observe a short DS in the first positions in both scenarios. However, in the Tokyo measurements this is even smaller due to the shorter street width. In Ilmenau there is a large yard at both sides of the street in the first three positions (see Fig. 3a) originating strong and late side reflections that increase the DS, visible in the PDPs in Fig. 6a and more specifically in Fig. 5a.

On the other hand, in both scenarios can be observed an increase with a subsequent decrease of the DS over TX-RX distance. This is caused by the reflection from Building B in Ilmenau, and Building D and back reflections in Tokyo. In the initial RX positions (short TX-RX distance), these reflections are not within the 20 dB DR. However, when the RX is moving closer to the building at the end of the street, the LOS component decreases due to the increased TX-RX distance, and the reflection becomes stronger due to the decrease on RX-back building distance. The maximum is reached in the position RX9 and RX10 in Ilmenau, and RX11 in Tokyo. After these positions, the difference of power between the LOS and reflected path becomes even smaller, but also the time difference between them, resulting on a subsequent decrease on DS. A similar behaviour is observed in the ASA in Fig. 8 due to the back reflections.

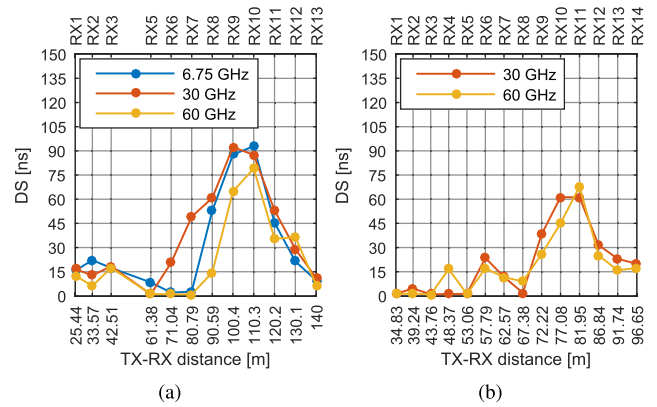


FIGURE 7. DS per position and per band calculated from the synthetic omni-directional PDP (a) in Ilmenau, and (b) in Tokyo.

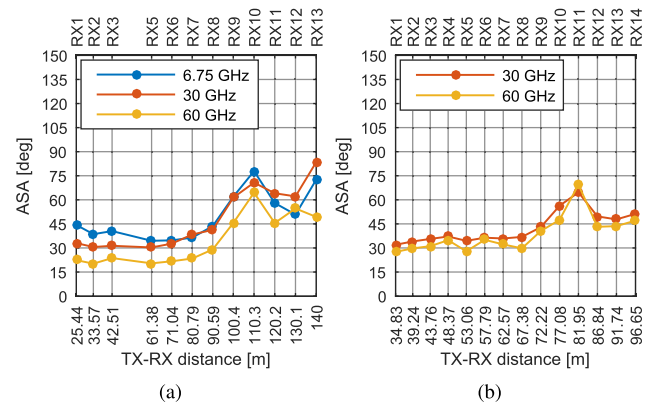


FIGURE 8. Per position and per band ASA at the RX in (a) Ilmenau, and (b) Tokyo.

C. ANGULAR DOMAIN CHARACTERIZATION

The per-position and per-band ASA in Ilmenau and Tokyo are shown in Fig. 8a and 8b, respectively. Similarly to what happens with the DS in Fig. 7, the ASA is also affected by the reflections from the buildings at the end of the street.

A slightly larger ASA can be observed in Ilmenau in the position RX1 when compared to Tokyo. This is due to the short TX-RX distances and larger street width (wide area between Building A and C in Fig. 3a): reflections from these buildings arrive from angles widely separated from the LOS. According the RX moves away from the TX, the reflections from the side buildings turn to arrive from angles closer to the LOS, and therefore the ASA slightly decreases up to the position RX6, in which the back reflection from the Building B starts to become more relevant. Since this reflection arrives almost 180° away from the LOS, the ASA values start to increase while the RX positions approach the Building B. Exactly the same trend in the ASA due to the reflection in the Building D at the end of the street can be observed in Tokyo, in the Fig. 8b.

On the other hand, as expected, the azimuth spread of departure (ASD) decreases with increasing TX-RX distance. In the RX positions closer to the TX, the TX reaches the RX

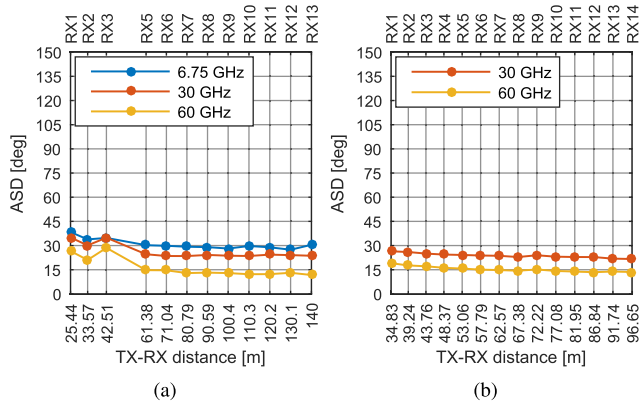


FIGURE 9. Per position and per band ASD at the RX in (a) Ilmenau, and (b) Tokyo.

with first order reflections from broad angles to the LOS, and conforming the RX moves away, the reflections angles start to get closer to the LOS.

The similar trend on the values along the RX displacement shows the similarities of the channel in the different bands. The mean and standard deviation of the ASs are summarized in Table 2. While the ASA is quite similar in both scenarios, the ASD is smaller in Tokyo.

D. MULTI-BAND EMPIRICAL PATH-LOSS

Path-loss describes the loss while the RX moves away from the source. The simplest empirical path-loss model is the close-in, which only counts with the path-loss exponent (PLE) α and uses as a reference the free-space path-loss (FSPL) at 1 m:

$$PL_{CI}(d, f_c) = 10\alpha \log_{10}(d) + 32.44 + 20 \log_{10}(f_c) + X_\sigma, \quad (8)$$

where d is the 3D TX-RX distance in meter, f_c is the carrier frequency in GHz, and $X_\sigma \sim \mathcal{N}(0, \sigma^2)$ is the shadowing factor.

On the other hand, the alpha-beta-gamma model (ABG) consists of three parameters: the PLE α , the reference path-loss at 1 m β (not necessarily FSPL), and a frequency dependent term γ :

$$PL_{ABG}(d, f_c) = 10\alpha \log_{10}(d) + \beta + 10\gamma \log_{10}(f_c) + X_\sigma, \quad (9)$$

It is worth to notice that by fixing $\beta = 32.44$ (FSPL at 1 m) and $\gamma = 2$ (PLE in FSPL) in (9), we obtain the close-in model in (8). While the ITU-R adopts the ABG model [3] in LOS, the 3GPP adopts the close-in in UMi street canyon scenarios under LOS [18].

The measured path-loss from the synthetic omni-directional channel in the Ilmenau and Tokyo street canyon scenarios and its fit to the ABG model (named as TUIL model, using the combined data-set) is displayed in Fig. 10. The parameters for the multi-band empirical path-loss

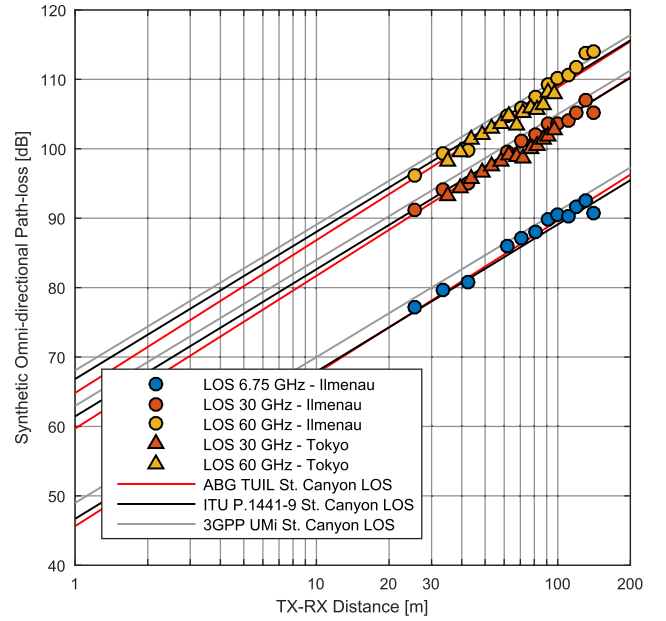


FIGURE 10. Measured synthetic omni-directional path-loss compared to the ITU and 3GPP street canyon models.

TABLE 1. Synthetic omni-directional path-loss: Measured and 3GPP and ITU-R street canyon models.

Model and measurements	α	β	γ	σ
ITU-R P.1441-9 Street Canyon	2.12	29.2	2.11	5.06
3GPP UMi Street Canyon	2.1	32.4	2	4
ABG Ilmenau (measured)	2.19	28.79	2.05	5.21
ABG Tokyo (measured)	1.95	31.93	2.09	2.80
ABG TUIL (measured)	2.2	28.96	2.01	4.49

obtained from the measurements in Ilmenau and Tokyo, independent and combined data-sets, are shown in Table 1.

In the Ilmenau scenario, the estimated multi-band PLE $\alpha = 2.19$, reference path-loss $\beta = 28.79$, and $\gamma = 2.05$ are within the range of the ones found in the literature [20], [21], and [31]. Hence, we can see a good match between our measurements and the 3GPP and ITU-R models. On the other hand, the PLE in Tokyo was estimated to $\alpha = 1.95$, which is slightly below 2. This can be caused by a stronger canyon effect due to the smaller street width (≈ 7.5 m) in comparison to Ilmenau (in average, ≈ 32 m).

The influence of the regularity of the buildings facades can also be seen in the standard deviation of the shadow fading, being higher in Ilmenau.

V. IDENTIFICATION AND MODELLING OF DETERMINISTIC COMPONENTS IN PROPAGATION CHANNELS

Since one of the main characteristics of communications at mm-waves is the utilization of beam-forming, channel models need to consider features as spatial consistency and accurate positioning of the scatterers in order to enable

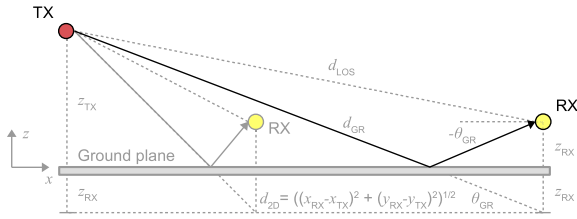


FIGURE 11. Schematic of the ground reflection.

simulation of directive systems. Such analysis is limited within GBSCMs as WINNER II and the SCM in the 3GPP that locate randomly the clusters in the environment.

While GR is not usually considered explicitly within GBSCMs, it is encouraged as an additional modelling component in the 3GPP models [18]. On the other hand, models as Millimetre-Wave Evolution for Backhaul and Access (MiWEBA) consider not only GR, but also other multiple deterministic clusters (generating the so-called D-rays) within the CIR [4].

In the following sub-sections we investigate the presence and relevance of GR and other side reflection (SR) that can be easily predicted in the measurements from the geometry of the scenario.

A. GROUND REFLECTION

GR is a deterministic component that is always present together with the LOS and becomes more visible when there is a large difference of height and distance between the BS and the UE. Depending on the system bandwidth and directivity (its capability of resolving it in time and direction), GRs can originate severe fading losses due to its proximity on time and DOA to the LOS component.

A sketch of the geometry of GR is displayed in Fig. 11, where $(x_{TX/RX}, y_{TX/RX}, z_{TX/RX})$ represents the TX and RX 3D Cartesian coordinates. The TOA of the GR path can be calculated as

$$\tau_{GR} = \frac{d_{GR}}{c} = \frac{\sqrt{(z_{TX} + z_{RX})^2 + d_{2D}^2}}{c}, \quad (10)$$

where d_{GR} is the GR path length, c is the speed of light, z_{TX} and z_{RX} are the TX and RX heights, respectively, and $d_{2D} = \sqrt{(x_{TX} - x_{RX})^2 + (y_{TX} - y_{RX})^2}$ is the 2D distance between the TX and RX. While the azimuth of arrival (AOA) of the GR path ϕ_{GR} equals the AOA of the LOS path ϕ_{LOS} , the elevation of arrival (EOA) θ_{GR} is calculated as

$$\theta_{GR} = -\arctan\left(\frac{z_{TX} + z_{RX}}{d_{2D}}\right), \quad (11)$$

$$\phi_{GR} = \phi_{LOS}.$$

The amplitude of the GR path is weighted by the reflection coefficient $\Gamma_{p,s}$ that depends on the polarization of the impinging wave, relative permittivity of the ground ϵ_{GR} , and incident angle θ_{GR} . The amplitude of the reflected paths in

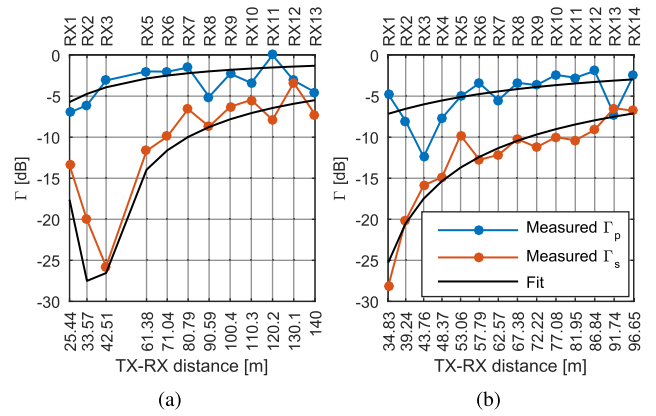


FIGURE 12. Measured reflection coefficient Γ_p (blue) and Γ_s (red) of the ground reflection at 30 GHz and its fit in (a) Ilmenau with $\epsilon_{GR} = 4.1$, and (b) Tokyo $\epsilon_{GR} = 2.3$.

the different polarizations is

$$\Gamma_p(\theta_{GR}) = \frac{\epsilon_{GR} \cos(\theta_{GR}) + \sqrt{\epsilon_{GR} - \sin^2(\theta_{GR})}}{\epsilon_{GR} \cos(\theta_{GR}) - \sqrt{\epsilon_{GR} - \sin^2(\theta_{GR})}},$$

$$\Gamma_s(\theta_{GR}) = \frac{\cos(\theta_{GR}) + \sqrt{\epsilon_{GR} - \sin^2(\theta_{GR})}}{\cos(\theta_{GR}) - \sqrt{\epsilon_{GR} - \sin^2(\theta_{GR})}}. \quad (12)$$

The RX power of the GR path (relative to the LOS) tracked in the measurements at 30 GHz in Ilmenau and Tokyo is shown in Fig. 12. The GR was extracted as the maximum component from the synthetic omni-directional PDP within a limited range estimated using (10). θ_{GR} is calculated using the set-up information and $\Gamma_{p,s}(\theta_{GR})$ are calculated by adjusting the permittivity and fitting the theoretical curve with the measurements. We can observe a good match between the predicted and measured power of the GR. Results reported in [16] have also shown that GR is the second strongest component apart from the LOS in street canyon scenarios.

B. SIDE AND BACK REFLECTIONS

A schematic of the street canyon scenario with a building at the end of the street is shown in Fig. 13. Depending on the location of the TX, sides reflections might occur on the left (SRL) and right (SRR) walls, taking as a reference the RX location. The propagation distance of the n^{th} order SRL $d_{SRL,n}$ and SRR $d_{SRR,n}$ can be calculated as

$$d_{SRL/SRR,n} = \sqrt{(x_{TX} - x_{RX})^2 + d_{y,SRL/SRR,n}^2 + (z_{TX} - z_{RX})^2}, \quad (13)$$

where $d_{y,SRL/SRR}$ is calculated as

$$d_{y,SRL,n} = \begin{cases} (n+1) \cdot w - y_{TX} - y_{RX} & \text{for odd } n \\ n \cdot w - y_{TX} + y_{RX} & \text{for even } n, \end{cases}$$

$$d_{y,SRR,n} = \begin{cases} (n-1) \cdot w + y_{TX} + y_{RX} & \text{for odd } n \\ n \cdot w + y_{TX} - y_{RX} & \text{for even } n. \end{cases} \quad (14)$$

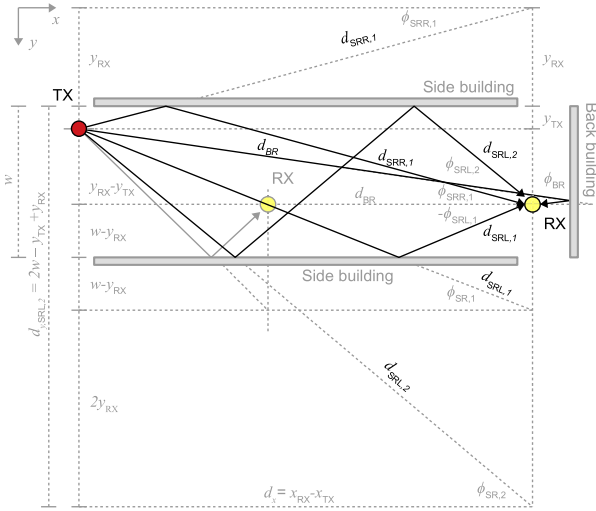


FIGURE 13. Schematic of the specular components in the canyon scenario with a building at the end.

On the other hand, the first order m^{th} back reflection (BR) distance can be estimated as

$$d_{BR,m} = \sqrt{(2 \cdot x_{BB,m} - x_{TX} - x_{RX})^2 + (d_{2D})^2}, \quad (15)$$

where $x_{BB,m}$ is the location of the m^{th} back scatterer in the x axis. The TOAs of these components can be calculated as $\tau_{SRL/SRR,n} = \frac{d_{SRL/SRR,n}}{c}$ and $\tau_{BR,m} = \frac{d_{BR,m}}{c}$. The AOA of the SR $\phi_{SRL/SRR,n}$ and BR $\phi_{BR,m}$ are calculated as

$$\begin{aligned} \phi_{RX,BR,m} &= 180 - \arctan\left(\frac{|y_{TX} - y_{RX}|}{|2 \cdot x_{BB,m} - x_{TX} - x_{RX}|}\right), \\ \phi_{RX,SRL,n} &= (-1)^n \arctan\left(\frac{|d_{y,SRL,n}|}{|x_{TX} - x_{RX}|}\right), \\ \phi_{RX,SRR,n} &= (-1)^{n+1} \arctan\left(\frac{|d_{y,SRR,n}|}{|x_{TX} - x_{RX}|}\right). \end{aligned} \quad (16)$$

The propagation distance of the strongest peaks from the synthetic omni-directional PDP in the different positions considering a dynamic range of 40 dB at 30 GHz and 60 GHz in Tokyo is displayed with crosses in Fig. 14a and 14b, respectively. The predicted propagation distance of the SRL up to third order and 5 different BRs (building at the end of the street, back wall of side building, etc.) is overlaid with circles. A very good match between the prediction of the cluster positions and the measurements can be observed.

On the other hand, Fig. 14a and Fig. 14d show the Ilmenau scenario at sub-6 GHz and 30 GHz, respectively. Due to the location of the TX, there are reflections from both sides. However, differently to the Tokyo scenario, third order reflections were only visible at some positions at sub-6 GHz but not at mm-waves. The influence of the street width w is also visible on the difference on propagation distance between the different reflection orders.

These clusters are mostly equally visible in the different bands. However, there are some positions in which the predicted clusters were shadowed in the measurements. This is

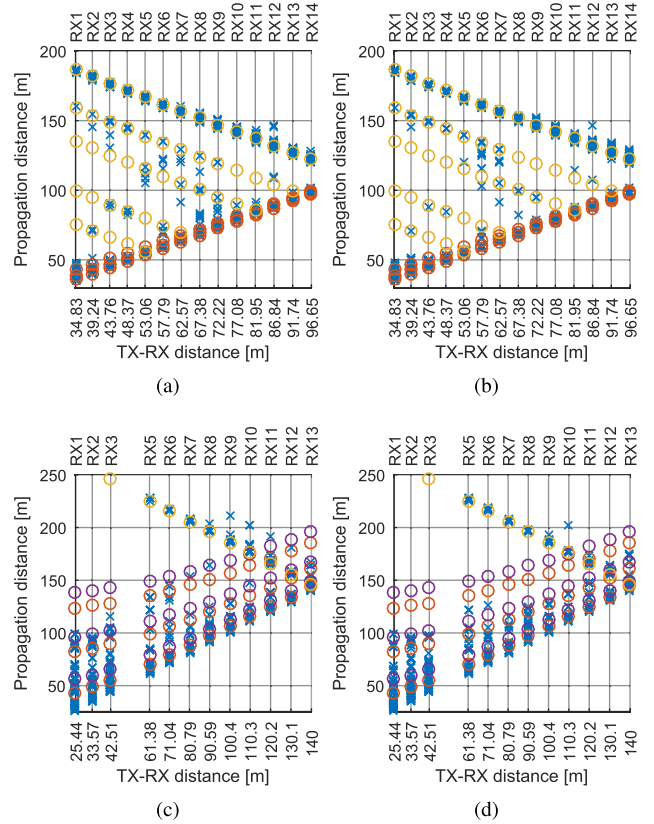


FIGURE 14. Measured (blue crosses) and estimated SRL (red circles), SRR (violet circles), and BR (orange circles) TOA of the specular components in the Tokyo scenario at (a) 30 GHz, (b) 60 GHz, in Ilmenau at (c) 6.75 GHz, and (d) 30 GHz.

because of the irregular facades of the buildings with different scattering properties and trees in the environment. The derivation of stochastic parameters to model the shadowing behaviour of the clusters that appear and disappear in the different positions is a future work.

Unfortunately, the angular characteristics cannot be contrasted with the measurements due to the coarse angular resolution of 30°.

While this approach allows to allocate the clusters in delay and angle, the scattering properties and distribution of the intra-clusters parameters as number of multi-path components, polarization, intra-cluster DSs, and intra-cluster ASs still need to be investigated with different tools due to the limitations on resolution of the measurement equipment and set-up presented in this paper.

C. DISCUSSIONS ON IMPLEMENTATION OF DETERMINISTIC COMPONENTS WITHIN GBSCMS

Deterministic components can be easily integrated in GBSCMs without burdening the computational complexity. In the proposed model, only the TX and RX locations are needed. Other components like the street width w and distances to the back reflection scatterers (buildings, cars, street signs) can be randomly generated on each

TABLE 2. List of large scale parameters from measurements.

		Propagation channel									Radio channel ¹				
		DS [ns]		ASA [deg]		ASD [deg]		PL (AB)			DS [ns]		PL (AB)		
Scenario	Band	Mean	Std.	Mean	Std.	Mean	Std.	α	β	σ	Mean	Std.	α	β	σ
Ilmenau	6.75 GHz	31.51	31.52	49.49	14.90	30.82	3.19	2.09	47.77	5.11	10.86	20.35	1.59	69.68	5.89
	30 GHz	37.69	30.48	48.29	18.84	26.25	4.44	2.06	62.29	5.02	5.78	12.60	1.72	80.47	6.49
	60 GHz	23.03	26.00	35.03	15.79	16.15	5.88	2.43	61.47	5.87	2.87	6.69	1.70	86.45	6.84
Tokyo	30 GHz	20.13	21.36	42.50	9.90	23.76	1.39	1.93	63.83	2.76	3.58	10.34	2.21	74.08	5.68
	60 GHz	18.27	18.77	38.53	11.32	15.30	1.47	2.04	67.25	2.94	2.62	7.50	2.28	79.15	5.77

¹ Considering directive antennas at TX and RX with 30° HPBW, and all the beams within a DR of 20 dB per-position.

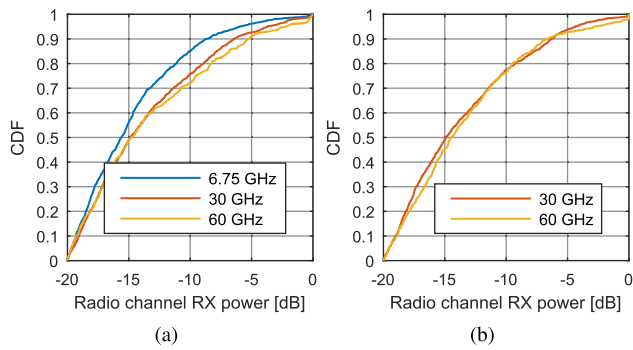


FIGURE 15. Cumulative density function of the radio channel power summarizing all the beams within 20 dB to the maximum of the different positions in (a) Ilmenau, and (b) Tokyo.

run to generate multiple different realizations of the channel. In addition, the inclusion of random clusters and visibility of the deterministic cluster in different positions can generate the variations of the channel observed during displacement.

The equations introduced in this section only provide the location in the angular and delay domain of the scatterer. The amplitude of the MPCs within the clusters has to be adjusted either from the LSPs or following a more deterministic criteria. While the latter is a more realistic approach, it doesn't necessarily guarantee LSPs consistent with measurements. However, we have seen that those deterministic components are defining the LSP.

VI. RADIO-CHANNEL CHARACTERIZATION

Since the antenna (or beam-former) is already considered within the radio channel, several modelling aspects as the location of clusters can be relaxed. Therefore, purely stochastic models derived from measurements are more suitable for this stage, in which parameters as the RX power and DS depends on the position and pointing direction of the beam-former. This directive characteristic can generate large losses when there is a mismatch on the beam pointing at TX and RX. Therefore, a pure LOS scenario contains two completely different situations: ALOS and NALOS.

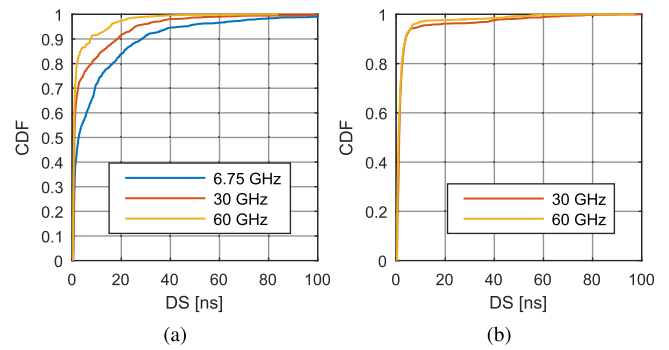


FIGURE 16. CDF of the DS_{RC} summarizing all the available beams within 20 dB to the maximum of the different positions in (a) Ilmenau, and (b) Tokyo.

We have characterized the radio channel by considering the patterns of the antennas used during the measurements as the output of beam-formers with the capability of steering fixed beams in the different measured directions. We assume a BS and UE with a codebook beam-former with 30° HPBWs. We have selected per-position all the pairs of TX-RX beams within a DR of 20 dB to the maximum. The mean and standard deviation of the DS and the AB path-loss model parameters are summarized in Table 2.

The CDF of the radio channel power is displayed in Fig. 15, showing very similar distributions in the different bands and scenarios. Therefore, we can claim that statistically there are similar opportunities in the different bands.

The severity of misalignment can be observed in Fig. 15, where the 50% of the cases showed a drop of 15 dB on RX power. However, it worth to notice that this includes only the pair of beams within 20 dB DR to the per-position maximum. If we consider all the possible beams, also the ones with no signal, we can observe that distributions vary considerable. The statistical characterization of available beams in the different frequencies, and the dependency on distance is part of future work.

The DS_{RC} is displayed in Fig. 16 for both scenarios, showing an inverse relation with the carrier frequency. In contrast to the RX power distributions in Fig. 15, the DS_{RC} shows a dependency on the scenario, being lower in Tokyo due to the shorter street width.

VII. CONCLUSION

In the present work we have introduced simultaneous multi-band measurements in street canyon scenarios in two different cities having completely different architectures: Ilmenau and Tokyo. The advantage of this measurement set-up, is that it allows a direct comparison of the propagation aspects at different bands. Since the same measurement equipment was utilized in the different locations, the differences on the channel depend purely on the characteristics of the environment.

From the propagation point of view, we have observed similarities on the synthetic omni-directional PDPs on the different bands and scenarios. This shows that the channel at mm-waves offers, in terms of scattering in a macro sense, similar opportunities than at sub-6 GHz. Therefore, the real challenge relies on the design of the appropriate radio interface to compensate the increased free space path-loss and to take advantage of these scatters.

We have found a high inter-band correlation on the shape of the evolution of the LSPs over the different positions. Furthermore, the comparison of the LSPs in Ilmenau and Tokyo shows similarities given purely by the architecture of the scenario: side buildings and a building at the end of the street. However, there are differences on the values in the different scenarios, which are mostly produced by the difference on the architecture: street width, facades, shape of buildings, etc.

In addition, the same specular components have been identified in the different bands and scenarios: ground and side reflections (up to third order in some locations), and multiple back reflections, showing that the channels are governed by a high deterministic behaviour that controls the LSPs. This facilitates the tracking and prediction of where to point the beam-formers.

However, GBSCMs following the system-level methodology as the SCM in 3GPP and its derivatives, fail to provide this consistency between the location of the scatterers and their TOA and DOA/DOD. Hence, while the inter-band similarities on LSPs let us think that models can be scaled in frequency, different modelling methodologies need to be followed in order to relate the angular and delay information of the clusters and increase accuracy on simulation of spatial characteristics for beam-forming and tracking.

The radio channel analysis (assuming a system with beam-forming) has shown the influence of the directivity on parameters as shadow fading and DS: the standard deviation of the RX power along the different positions and the DS was drastically reduced when the radio interfaces were aligned (ALOS). Contrarily, the analysis of the NALOS channel has shown large variations on RX power and DS. In that regard, we have introduced stochastic models derived from the measurements to predict RX power and DS considering the situation in which the BS and UE are not always aligned.

REFERENCES

- [1] S. Salous, V. D. Esposti, F. Fuschini, R. S. Thomae, R. Mueller, D. Dupleich, K. Haneda, J.-M. M. Garcia-Pardo, J. P. Garcia, D. P. Gaillot, S. Hur, and M. Nekovee, "Millimeter-wave propagation: Characterization and modeling toward fifth-generation systems. [Wireless Corner]," *IEEE Antennas Propag. Mag.*, vol. 58, no. 6, pp. 115–127, Dec. 2016. doi: [10.1109/MAP.2016.2609815](https://doi.org/10.1109/MAP.2016.2609815).
- [2] M. Rumney, P. Kyösti, and L. Hentilä, "3GPP channel model developments for 5G NR requirements and testing," in *Proc. 12th Eur. Conf. Antennas Propag. (EuCAP)*, London, U.K., Apr. 2018, pp. 1–5. doi: [10.1049/cp.2018.0877](https://doi.org/10.1049/cp.2018.0877).
- [3] *Propagation Data and Prediction Methods for the Planning of Short-Range Outdoor Radiocommunication Systems and Radio Local Area Networks in the Frequency Range 300 MHz to 100 GHz*, document ITU-R, ITU-R P.1411-9, 2017. [Online]. Available: <https://www.itu.int/rec/R-REC-P.1411/en>
- [4] R. J. Weiler, M. Peter, W. Keusgen, A. Maltsev, I. Karls, A. Pudueyev, I. Bolotin, I. Sjaud, and A.-M. Ulmer-Moll, "Quasi-deterministic millimeter-wave channel models in MiWEBA," *EURASIP J. Wireless Commun. Netw.*, vol. 2016, p. 84, Mar. 2016. doi: [10.1186/s13638-016-0568-6](https://doi.org/10.1186/s13638-016-0568-6).
- [5] *Measurement Results and Final mmMAGIC Channel Models*, document H2020-ICT-671650-mmMAGIC/D2.2 Deliverable D2.2, 2017. [Online]. Available: <https://5g-mmmagic.eu/results/#deliverables>
- [6] V. Nurmela. (2015). *METIS Channel Models: Deliverable D1.4*. [Online]. Available: <https://metis2020.com/documents/deliverables/index.html>
- [7] D. Dupleich, E. Schäfer, G. D. Galdo, R. Thomä, "Influence of system aspects in propagation based evaluation of beam-forming at mm-waves," in *Proc. 12th Eur. Conf. Antennas Propag. (EuCAP)*, London, U.K., Apr. 2018, pp. 1–5. doi: [10.1049/cp.2018.0763](https://doi.org/10.1049/cp.2018.0763).
- [8] S. Kuttu and D. Sen, "Beamforming for millimeter wave communications: An inclusive survey," *IEEE Commun. Surveys Tuts.*, vol. 18, no. 2, pp. 949–973, 2nd Quart., 2016. doi: [10.1109/COMST.2015.2504600](https://doi.org/10.1109/COMST.2015.2504600).
- [9] D. Dupleich, J. Luo, S. Haefner, R. Mueller, C. Schneider, and R. Thomae, "A hybrid polarimetric wide-band beam-former architecture for 5G mm-wave communications," in *Proc. 20th Int. ITG Workshop Smart Antennas*, Munich, Germany, 2016, pp. 1–8.
- [10] D. Dupleich, N. Iqbal, C. Schneider, S. Häfner, R. Müller, S. Skoblikov, J. Luo, G. D. Galdo, and R. Thomä, "Influence of system aspects on fading at mm-waves," *IET Microw., Antennas Propag.*, vol. 12, no. 4, pp. 516–524, 2018. doi: [10.1049/iet-map.2017.0601](https://doi.org/10.1049/iet-map.2017.0601).
- [11] D. Dupleich, F. Fuschini, R. Mueller, E. Vitucci, C. Schneider, V. D. Esposti, R. Thomä, "Directional characterization of the 60 GHz indoor-office channel," in *Proc. 31st URSI General Assem. Sci. Symp. (URSI GASS)*, Beijing, China, 2014, pp. 1–4. doi: [10.1109/URSIGASS.2014.6929648](https://doi.org/10.1109/URSIGASS.2014.6929648).
- [12] D. Dupleich, R. Müller, N. Han, S. Häfner, C. Schneider, J. Luo, G. D. Galdo, and R. S. Thomä, "Polarization in spatial channel models at mm-Waves: A correlation based approach," in *Proc. 13th Eur. Conf. Antennas Propag. (EuCAP)*, Krakow, Poland, 2019, pp. 1–5.
- [13] S. Wu, S. Hur, K. Whang, and M. Nekovee, "Intra-cluster characteristics of 28 GHz wireless channel in urban micro street canyon," in *Proc. IEEE Global Commun. Conf. (GLOBECOM)*, Washington, DC, USA, Dec. 2016, pp. 1–6. doi: [10.1109/GLOCOM.2016.7841916](https://doi.org/10.1109/GLOCOM.2016.7841916).
- [14] L. Liu, C. Oestges, J. Poutanen, K. Haneda, P. Vainikainen, F. Quitin, F. Tufvesson, and P. De Doncker, "The COST 2100 MIMO channel model," *IEEE Wireless Commun.*, vol. 19, no. 6, pp. 92–99, Dec. 2012.
- [15] P. Kyosti. (2007). *WINNER II Channel Models: IST-4-027756 WINNER II D1.1.2 V1.1*. [Online]. Available: <http://www.ist-winner.org/WINNER2-Deliverables/D1.1.2v1.1.pdf>
- [16] A. Maltsev. (2014). *MiWEBA D5.1: Channel Modelling and Characterization*. [Online]. Available: <https://www.miweba.eu/#Publications>
- [17] B. Peng, K. Guan, S. Rey, T. Kürner, "Two-step angle-of-arrival estimation for terahertz communications based on correlation of power-angular spectra in frequency," in *Proc. 12th Eur. Conf. Antennas Propag. (EuCAP)*, London, U.K., 2018, pp. 1–5. doi: [10.1049/cp.2018.0759](https://doi.org/10.1049/cp.2018.0759).
- [18] European Telecommunications Standards Institute. (2018). *Study on Channel Model for Frequencies From 0.5 to 100 GHz: 3GPP TR 38.901 Version 15.0.0 Release 15*. [Online]. Available: <http://www.etsi.org>
- [19] S. L. H. Nguyen, J. Järveläinen, A. Karttunen, K. Haneda, and J. Putkonen, "Comparing radio propagation channels between 28 and 140 GHz bands in a shopping mall," in *Proc. 12th Eur. Conf. Antennas Propag. (EuCAP)*, London, U.K., 2018, pp. 1–5. doi: [10.1049/cp.2018.0874](https://doi.org/10.1049/cp.2018.0874).

- [20] X. Raimundo, S. El-Faitori, and S. Salous, "Multi-band outdoor measurements in a residential environment for 5G networks," in *Proc. 12th Eur. Conf. Antennas Propag. (EuCAP)*, London, U.K., 2018, pp. 1–4. doi: [10.1049/cp.2018.0727](https://doi.org/10.1049/cp.2018.0727).
- [21] M. Sasaki, M. Nakamura, W. Yamada, N. Kita, Y. Takatori, M. Inomta, K. Kitao, and T. Imai, "Path loss characteristics from 2 to 66 GHz in urban macrocell environments based on analysis using ITU-R site-general models," in *Proc. 12th Eur. Conf. Antennas Propag. (EuCAP)*, London, U.K., 2018, pp. 1–5. doi: [10.1049/cp.2018.0726](https://doi.org/10.1049/cp.2018.0726).
- [22] T. S. Rappaport, F. Gutierrez, Jr., E. Ben-Dor, J. N. Murdock, Y. Qiao, and J. I. Tamir, "Broadband millimeter-wave propagation measurements and models using adaptive-beam antennas for outdoor urban cellular communications," *IEEE Trans. Antennas Propag.*, vol. 61, no. 4, pp. 1850–1859, Apr. 2013. doi: [10.1109/TAP.2012.2235056](https://doi.org/10.1109/TAP.2012.2235056).
- [23] T. S. Rappaport, S. Sun, R. Mayzus, H. Zhao, Y. Azar, K. Wang, G. N. Wong, J. K. Schulz, M. Samimi, and F. Gutierrez, "Millimeter wave mobile communications for 5G cellular: It will work!" *IEEE Access*, vol. 1, pp. 335–349, May 2013. doi: [10.1109/ACCESS.2013.2260813](https://doi.org/10.1109/ACCESS.2013.2260813).
- [24] T. S. Rappaport, G. R. Maccartney, M. K. Samimi, and S. Sun, "Wide-band millimeter-wave propagation measurements and channel models for future wireless communication system design," *IEEE Trans. Commun.*, vol. 63, no. 9, pp. 3029–3056, Sep. 2015. doi: [10.1109/TCOMM.2015.2434384](https://doi.org/10.1109/TCOMM.2015.2434384).
- [25] S. Hur, S. Baek, B. Kim, Y. Chang, A. F. Molisch, T. S. Rappaport, K. Haneda, and J. Park, "Proposal on millimeter-wave channel modeling for 5G cellular system," *IEEE J. Sel. Topics Signal Process.*, vol. 10, no. 3, pp. 454–469, Apr. 2016. doi: [10.1109/JSTSP.2016.2527364](https://doi.org/10.1109/JSTSP.2016.2527364).
- [26] R. J. Weiler, M. Peter, T. Kühne, M. Wisotzki, and W. Keusgen, "Simultaneous millimeter-wave multi-band channel sounding in an urban access scenario," in *Proc. 9th Eur. Conf. Antennas Propag. (EuCAP)*, Lisbon, Portugal, 2015, pp. 1–5.
- [27] R. Müller, S. Häfner, D. Dupleich, R. S. Thomä, G. Steinböck, J. Luo, E. Schulz, X. Lu, and G. Wang, "Simultaneous multi-band channel sounding at mm-Wave frequencies," in *Proc. 10th Eur. Conf. Antennas Propag. (EuCAP)*, Davos, Switzerland, 2016, pp. 1–5. doi: [10.1109/EuCAP.2016.7481757](https://doi.org/10.1109/EuCAP.2016.7481757).
- [28] D. Dupleich, R. Müller, S. Skoblikov, C. Schneider, J. Luo, G. D. Galdo, and R. Thomä, "Multi-band indoor propagation characterization by measurements from 6 to 60 GHz," in *Proc. 13th Eur. Conf. Antennas Propag. (EuCAP)*, Krakow, Poland, 2019, pp. 1–5.
- [29] M. Boban, D. Dupleich, N. Iqbal, J. Luo, C. Schneider, R. Müller, Z. Yu, D. Steer, T. Jämsä, J. Li, and R. S. Thomä, "Multi-band vehicle-to-vehicle channel characterization in the presence of vehicle blockage," *IEEE Access*, vol. 7, pp. 9724–9735, 2019. doi: [10.1109/ACCESS.2019.2892238](https://doi.org/10.1109/ACCESS.2019.2892238).
- [30] R. Müller, R. Herrmann, D. A. Dupleich, C. Schneider, and R. S. Thomä, "Ultrawideband multichannel sounding for mm-wave," in *Proc. 8th Eur. Conf. Antennas Propag. (EuCAP)*, The Hague, Netherlands, 2014, pp. 817–821. doi: [10.1109/EuCAP.2014.6901887](https://doi.org/10.1109/EuCAP.2014.6901887).
- [31] S. Sun, T. S. Rappaport, T. A. Thomas, A. Ghosh, H. C. Nguyen, I. Z. Kovács, I. Rodriguez, O. Koymen, and A. Partyka, "Investigation of prediction accuracy, sensitivity, and parameter stability of large-scale propagation path loss models for 5G wireless communications," *IEEE Trans. Veh. Technol.*, vol. 65, no. 5, pp. 2843–2860, May 2016. doi: [10.1109/TVT.2016.2543139](https://doi.org/10.1109/TVT.2016.2543139).

• • •